

# High redshift radio quiet quasars - exploring the parameter space of accretion models. Part I: hot semi-spherical flow

Małgorzata A. Sobolewska

*Harvard-Smithsonian Center for Astrophysics, Cambridge, MA 02138*

*Nicolaus Copernicus Astronomical Center, 00-716 Warsaw, Poland*

msobolewska@cfa.harvard.edu, malsob@camk.edu.pl

Aneta Siemiginowska

*Harvard-Smithsonian Center for Astrophysics, Cambridge, MA 02138*

asiemiginowska@cfa.harvard.edu

and

Piotr T. Życki

*Nicolaus Copernicus Astronomical Center, 00-716 Warsaw, Poland*

ptz@camk.edu.pl

## ABSTRACT

Two families of models are currently considered to describe an accretion flow onto black holes and production of the observed X-ray radiation: (1) a standard cold accretion disk with a hot corona above it and (2) an outer truncated accretion disk with a hot semispherical inner flow. We compute spectra in the scenario with a hot inner flow surrounded by a truncated accretion disk covered by a hot corona and test the results on a sample of high redshift ( $z > 4$ ) quasars observed with *Chandra*. We find that in order to reproduce the ratio of optical to X-ray fluxes (the  $\alpha_{\text{ox}}$  parameter), the optical depth of the Comptonizing plasma has to be rather low ( $\tau = 0.02 - 0.15$  in the corona above the disk, and  $\tau = 0.15 - 0.70$  in the hot inner flow). This, together with the observed X-ray photon indices, implies either a high temperature in a thermal plasma ( $kT_e = 90 - 500$  keV), or a nonthermal electron distribution in the plasma. We put an upper limit on the disk truncation radius,  $r_{\text{tr}} \leq 40R_S$ . The modeled accretion rate is high,  $\dot{m} > 0.2 \dot{M}_{\text{Edd}}$ , which may suggest that high- $z$  radio quiet quasars are analogs of X-ray binaries in their high or very high state.

*Subject headings:* accretion, accretion disks — galaxies: high-redshift — quasars: general — X-Rays

## 1. Introduction

Modern X-ray observatories can detect the most distant objects in the universe and provide high quality data for quasars at redshifts as high as  $\sim 6$  (Becker et al. 2001; Brandt et al. 2002b; Bechtold et al. 2003, hereafter B03), i.e. for objects born in the very early universe. By comparing high- and low-redshift sources, we may be able to determine whether these objects evolve and if there is any particular pattern that they follow during the evolution. This provides bases for studying the formation and evolution of the universe.

We focus our studies on the radio quiet quasars (RQQs), which comprise  $\sim 85\% - 90\%$  of the quasar population (e.g., Stern et al. 2000). The fact that RQQs are more common, and thus more typical, among the quasars makes it important to understand the origin of their broad-band spectra. In these systems a contribution from possible additional components related to the radio emission should be negligible. On the other hand, RQQs are X-ray quieter than radio loud quasars (RLQs) in terms of higher  $\alpha_{\text{ox}}$  parameter — the spectral index of a reference power law connecting the optical and X-ray rest frame fluxes, for which we use the following definition:  $\alpha_{\text{ox}} = -(\log f_x - \log f_o) / (\log \nu_x - \log \nu_o)$ , where  $f_o$  and  $f_x$  are rest frame optical and X-ray fluxes at  $\lambda = c/\nu_o = 2500 \text{ \AA}$  and  $E = h\nu_x = 2 \text{ keV}$  (e.g., Zamorani et al. 1981; Worrall et al. 1987; Laor et al. 1997) — so the X-ray data of RQQs are of worse quality than those of RLQs.

Understanding observed spectral features in terms of theoretical model parameters can provide important insights into physical processes taking place in quasars, especially about the origins of the hard X-ray radiation. The “standard” model so far successful in explaining optical/UV/X-ray spectra of active galactic nuclei (AGNs) (and those of X-ray binaries, hereafter XRBs) contains as a crucial element an optically thick accretion disk around a central black hole. Gravitational energy is dissipated and thermalized in the accretion disk (Shakura & Sunyaev 1973). It is emitted in the form of thermal radiation, giving a characteristic bump in the optical/UV band (“big blue bump”) in AGN spectra (Shields 1978, Czerny & Elvis 1987, Siemiginowska et al. 1995, Koratkar & Blaes 1999) or soft X-rays in the case of XRBs (see, e.g., a review by McClintock & Remillard 2003). In the case of high- $z$  RQQs, the central black hole is expected to be supermassive, with a mass of up to  $\sim 10^{10} M_\odot$  (Rees 1984). Such a high mass is suggested by the high luminosities of high- $z$  RQQs (of the order of  $\sim 10^{48} \text{ ergs s}^{-1}$ ), which should not exceed the Eddington luminosity of  $L_{\text{Edd}} \approx 1.3 \times 10^{46} (M/10^8 M_\odot) \text{ erg s}^{-1}$ .

Some of the disk photons gain energy in the inverse Compton process by scattering off energetic electrons in a hot, optically thin plasma. This mechanism is generally accepted to explain hard power-law-like spectral X-ray tails extending beyond 100 keV (see Mushotzky, Done & Pounds 1993 for a review; Done 2001). The spectra commonly show cut-offs beyond

$\sim 100$  keV in both Seyfert galaxies and XRB (in their hard/low states), suggesting a thermal energy distribution of Comptonizing electrons (Gierliński et al. 1997, Zdziarski et al. 1998). Observed X-ray spectra of XRBs (soft/high states) may extend to energies beyond 500 keV (e.g., Gierliński et al. 1999) with no cut-off, implying a non-thermal energy distribution or, possibly, a hybrid (i.e., a mixture of thermal and non-thermal; Coppi 1999) electron distribution.

Some of the Comptonized X-ray photons are likely to illuminate the accretion disk, where they can be reprocessed and mostly thermalized, thus increasing the disk flux. Since the disk flux provides the seed photons for the inverse Compton processes, a feedback loop between the cold disk and the hot plasma is created (Haardt & Maraschi 1991, 1993).

Some of the illuminating X-ray photons will be reflected by Compton scattering off cold electrons and emerge back from the disk, with a characteristic spectrum (Lightman & White 1988; George & Fabian 1991). The spectrum is composed of (1) a broad continuum (“reflection hump”) peaking at 20–30 keV, whose shape is determined by a competition between photo-absorption in the soft X-ray band ( $E < 10$  keV) and Klein-Nishina effects on the Compton scattering cross-section in the hard X-ray band, (2) the Fe  $K_\alpha$  fluorescence/recombination line at 6.4–6.97 keV (depending on the Fe ionization state), and (3) the Fe- $K_\alpha$  edge at  $\sim 7.1$ –10 keV. The fluorescence features can be further influenced by relativistic effects and/or the ionization state of the reflecting medium (Fabian et al. 1989; Życki & Czerny 1994, Nayakshin 2000).

An unresolved issue is that of the geometry of the accretion flow, i.e., a geometrical configuration of the two phases of accreting plasma (cold, optically thick; and hot, optically thin). There are two general scenarios considered in the modeling: (1) the plane-parallel geometry, in which a hot corona is located atop the accretion disk, which is assumed to extend down to the innermost stable orbit ( $r_{\text{in}} = 3 R_S$  for a Schwarzschild black hole, where Schwarzschild radius  $R_S \equiv 2GM/c^2$ ), and (2) the spherical geometry, which assumes that the cold disk is truncated at a certain radius  $r_{\text{tr}} > r_{\text{in}}$  and surrounds a hot inner plasma flow within  $r < r_{\text{tr}}$  (Shapiro et al. 1976; Poutanen et al. 1997; Esin, McClintock & Narayan 1997; Różańska & Czerny 2000). In the first geometry, the hot corona sandwiching the disk may be continuous (e.g., Haardt & Maraschi 1991) or “patchy” i.e., composed of a number of active regions driven by, e.g., magnetic activity (Galeev, Rosner & Vaiana 1979). A variant of the spherical geometry (case 2 above) is the spherical cloud model of Collin-Souffrin et al. (1996), in which the cold plasma forms small clouds accreting roughly spherically onto the central X-ray source.

In principle, one can distinguish between the two basic geometries by studying the X-ray spectrum in detail (see Done 2001 for a review). One argument is based on the amplitude

of the reflection component. The amplitude is defined as

$$R \equiv \Omega/2\pi, \quad (1)$$

where  $\Omega$  is a solid angle subtended by the reflector as seen from the source of X-rays. For plane-parallel geometry,  $R$  should yield values close to unity (the disk covers  $\approx 2\pi$  from the point of view of the X-ray source), whereas for spherical geometry  $R < 1$  would be expected. Furthermore, the amount of broadening of the reflection features gives an estimate of the inner radius of the accretion disk (e.g., Done et al. 2000). For example, the Fe  $K\alpha$  line would be narrower if the disk were truncated far away from  $r_{\text{in}}$ .

Another argument in determining the geometry may be based on the X-ray photon index,  $\Gamma$ . A continuous, plane-parallel corona produces rather soft X-ray spectrum,  $\Gamma > 2$ , even when the entire gravitational energy is dissipated in the corona (Haardt & Maraschi 1991, 1993). This is because the underlying cold disk provides a lower limit to the cooling flux. The spectra in the spherical geometry are harder,  $\Gamma < 2$ , because the disk flux entering the central sphere is strongly reduced, compared to that in the plane-parallel geometry (e.g., Poutanen et al. 1997).

However, these diagnostics do not determine the geometry in a unique way, since it is possible to modify the continuous plane-parallel corona scenario in such a way that the predicted spectra are hard, with  $\Gamma < 2$ , and the amplitude of reflection is reduced,  $R < 1$ . This may be realized in a number of scenarios: (1) the hot plasma may form a patchy corona (Stern et al. 1995); (2) the cold disk may be covered by a hot ionized skin, decreasing the effectiveness of the reprocessing/thermalization (Nayakshin, Kazanas & Kallman 2000); or (3) the hot plasma may be outflowing at relativistic speeds, so that relativistic beaming makes the emission pattern significantly anisotropic (Beloborodov 1999a). In particular, both the spherical geometry scenario and models 2 and 3 above, reproduce the correlation observed between the X-ray spectral index and amplitude of reflection of both Seyfert galaxies and XRB (Zdziarski et al. 1999).

An additional model diagnostic, which helps to break the degeneracy, is the ratio of observed optical and X-ray fluxes, the X-ray loudness,  $\alpha_{\text{ox}}$ . This parameter is of more use for AGNs than for XRBs, since the disk emission can be more easily observed in AGNs than in XRBs. This is especially true for high- $z$  quasars, where the big blue bump may be redshifted into the observable optical band. On the other hand, the quality of X-ray data from these objects is usually not sufficient to accurately determine the amplitude of the reprocessed component (see Siebert et al. 1996, Lawson & Turner 1997, Cappi et al. 1997, Reeves & Turner 2000, Mineo et al. 2000, and Page et al. 2003 for attempts to fit reflected component and/or iron  $K\alpha$  line to the data of quasars).

The “complex” models described above were applied to Seyfert galaxies and low redshift RQQs with high S/N (signal-to-noise ratio) data (recently, e.g., by Chiang 2002; Chiang & Blaes 2003; Janiuk, Czerny & Madejski 2001). So far the quasars’ spectral energy distribution, especially that of high redshift quasars, has been modeled by the thermal emission from an accretion disk (Sun & Malkan 1989, Bechtold et al. 1994a, 1994b, Tripp et al. 1994), with the addition of a Comptonizing medium explaining the X-rays (Band & Malkan 1988, Fiore et al. 1995). There have been no systematic studies of the parameter space of these models appropriate for high- $z$  quasars, while the number of the observations has been increasing.

In this paper we consider a geometry with a hot inner flow surrounded by a truncated accretion disk covered with a hot corona. We apply the model to the high redshift RQQs. Similar geometry was applied by Chiang (2002) and Chiang & Blaes (2003) to Seyfert galaxies. Their Compton scattering medium was located within the central sphere, which was surrounded by an accretion disk. They extended the model of Zdziarski et al. (1999) by introducing viscous dissipation in the cold disk and modeled X-ray data simultaneously with the optical/UV data. In our model we include two Comptonizing media, the sphere and the corona. We explore the model parameter space and identify the model parameters suitable to generate the observed spectra of RQQs. The observational constraints include three quantities: the X-ray photon index,  $\Gamma$ , the X-ray loudness,  $\alpha_{\text{ox}}$ , and the optical/UV luminosity,  $l_{\text{UV}} \equiv \log(\nu L_\nu)$  at 2500 Å in the rest frame. Optical/UV luminosities of high- $z$  RQQs are of the order of  $l_{\text{UV}} \gtrsim 46.0\text{--}47.0$  (B03 and references therein). B03 and Vignali et al. (2003a, hereafter V03; 2003b) derived the mean  $\sim 2\text{--}30$  keV rest frame X-ray photon index to be in the range  $\sim 1.5\text{--}2$ . The X-ray loudness was found to be  $\sim 1.7\text{--}1.8$  (B03; V03; Vignali et al. 2003b).

The structure of the paper is as follows: In Section 2, we describe the geometry of accretion flow and describe the model. In Section 3, we present the results of computations, and discuss the constraints imposed on the parameter space by the observations. In Section 4, we apply the spherical geometry accretion model to the high- $z$  RQQ data of B03. Finally, Sections 5 and 6 contain discussion and concluding remarks, respectively.

In a subsequent paper (Sobolewska et al. 2004, hereafter Paper II), we study the accretion disk model covered by a non-uniform corona composed from hot clouds (a patchy corona).

## 2. Model

We consider an accretion flow consisting of (1) a cold, optically thick accretion disk with (2) a hot corona above it. At a radius  $r_{\text{tr}}$  greater than the radius of the innermost stable orbit,  $r_{\text{in}}$ , the disk evaporates completely to (3) a hot inner flow. The geometry is schematically presented in Figure 1. The computed spectra are a superposition of the thermal disk radiation that escapes the hot plasma (both the corona and the inner flow) without being scattered, and the Comptonized component. The spectra are computed in a face-on view.

Throughout the paper we assume the Schwarzschild geometry, the innermost stable circular orbit is located at  $r_{\text{in}} = 3R_{\text{S}}$ , where  $R_{\text{S}} = \frac{2GM}{c^2}$ , and the accretion efficiency is  $\epsilon=1/12$  (unless stated otherwise). We define the Eddington accretion rate as  $\epsilon\dot{M}_{\text{Edd}}c^2 = 1.3 \times 10^{46} \frac{M}{10^8 M_{\odot}}$  ergs s<sup>-1</sup> and use the unitless quantity  $\dot{m} = \dot{M}/\dot{M}_{\text{Edd}}$  to describe the accretion rate.

### 2.1. The disk component

At each radius  $r > r_{\text{tr}}$ , we assume that the hot corona above the accretion disk dissipates a fraction  $f$  of the locally released gravitational energy and that the remaining energy is dissipated in the disk.

The total dissipative luminosity available between the innermost stable circular orbit,  $r_{\text{in}}$ , and the transition radius,  $r_{\text{tr}}$ , is

$$L_{\text{available}} = 4\pi \int_{r_{\text{in}}}^{r_{\text{tr}}} F_{\text{visc}}(r)rdr, \quad (2)$$

where  $F_{\text{visc}}(r) = \frac{3GM\dot{M}}{8\pi r^3} \left(1 - \sqrt{\frac{r_{\text{in}}}{r}}\right)$ . We calculate the total luminosity dissipated in the hot inner flow as

$$L_{\text{diss}} = \delta L_{\text{available}}, \quad (3)$$

where  $0 < \delta < 1$  is the radiation efficiency correction to the Keplerian efficiency within the inner flow.

The cold disk ( $r > r_{\text{tr}}$ ) is illuminated by both the hot inner flow and the hot corona. Part of this illuminating flux is reprocessed in the disk. Therefore, at each radius three contributions account for the total accretion disk soft flux: (1) viscous dissipation in the disk, (2) reprocessing of the hard coronal radiation, and (3) reprocessing of the hard radiation

originating in the inner flow (see Figure 1). The total soft disk flux is thus given by

$$\begin{aligned}
 F_{\text{soft}}(r) &= (1 - f)F_{\text{visc}}(r) + f\eta(1 - a)F_{\text{visc}}(r) + \\
 &+ (1 - a)F_{\text{inc}}(r),
 \end{aligned}
 \tag{4}$$

where  $a$  and  $\eta$  are the energy-integrated disk albedo and the Compton anisotropy parameter (Haardt & Maraschi 1991), respectively (we assume typical values of  $a = 0.2$  and  $\eta = 0.5$ ; Haardt & Maraschi 1993), while  $(1 - a)F_{\text{inc}}(r)$  is the flux from the inner flow intercepted by the disk annulus at  $r$  and  $F_{\text{inc}}(r) = \frac{3L_{\text{diss}}}{16\pi^2 r_{\text{tr}}^2 r_s} \int_0^{\alpha_{\text{max}}} \sin \alpha \cos \alpha d\alpha \int_{-\phi_{\text{max}}}^{\phi_{\text{max}}} l d\phi$  (Chiang 2002). For completeness, we give expressions for  $\alpha_{\text{max}}$ ,  $\phi_{\text{max}}$ , and  $l(r, \alpha, \phi, r_s)$  in the Appendix. Derivation of  $F_{\text{inc}}$  was performed for a uniform, isotropically radiating inner flow.

We assume that in the disk/corona region the accretion disk radiates locally as a blackbody with a temperature  $T = (F_{\text{soft}}/\sigma_{\text{SB}})^{1/4}$ , where  $\sigma_{\text{SB}}$  is the Stefan-Boltzmann constant, and  $F_{\text{soft}}$  is given by equation (4). This local disk emission is Comptonized in the corona. The input spectrum for the Comptonization in the inner flow is determined as a superposition of local blackbodies originating in the disk at radii  $r_i$ , between  $r_{\text{tr}}$  and  $r_{\text{out}}$ , chosen arbitrarily to be  $10^5 R_{\text{S}}$ . Each contributing blackbody is normalized to the luminosity intercepted by the inner flow from a given radius,  $L_{\text{soft}}(r_i)$ , given by

$$L_{\text{soft}}(r_i) = 4\pi \int_{r_i}^{r_{i+1}} g(r) \frac{F_{\text{soft}}(r)}{\pi} r dr,
 \tag{5}$$

where  $g(r)$  is a geometrical factor (Chiang 2002; see also the Appendix). These contributions sum to the total disk luminosity intercepted by the hot inner flow, i.e.,

$$L_{\text{soft}} = \sum_{r_i} L_{\text{soft}}(r_i).
 \tag{6}$$

## 2.2. The Comptonized component

In order to compute the Comptonized component, we use the empirical formulas of Beloborodov (1999b) that relate the amplification factor,  $A$ , the photon index,  $\Gamma$ , and the Compton parameter,

$$y = 4\theta_e(1 + 4\theta_e)\tau(1 + \tau)
 \tag{7}$$

(where  $\theta_e = kT_e/m_e c^2$ ):

$$\Gamma = \frac{7}{3}(A - 1)^{-1/10},
 \tag{8}$$

$$\Gamma = \frac{9}{4}y^{-2/9}.
 \tag{9}$$



In general, the amplification factor is defined as follows:

$$A = \frac{L_{\text{soft}} + L_{\text{diss}}}{L_{\text{soft}}}, \quad (10)$$

where  $L_{\text{diss}}$  stands for the total luminosity dissipated in the hot plasma and  $L_{\text{soft}}$  denotes the soft luminosity that enters the hot plasma from the accretion disk.

We perform our analysis for electron temperatures in the hot plasma of  $kT_e = 150$  and 500 keV. We compute the optical depth of the plasma,  $\tau$ , and the photon index,  $\Gamma$ , combining equations (7), (8), and (9).

The relative strengths of the power-law-like high energy tail and the soft input spectrum escaping the hot plasma without any shift in the energy are determined by the probability,  $P_\tau$ , that a soft photon is scattered to a higher energy in the Comptonization process. To calculate  $P_\tau$ , we use the formula

$$\Gamma - 1 = -\frac{\ln P_\tau}{\ln \Delta E}, \quad (11)$$

where  $\Gamma$  is the photon index ( $\Gamma - 1$  is the spectral index) and  $\Delta E = 1 + 4\theta_e(1 + 4\theta_e)$  denotes the mean energy amplification in a Thomson collision.

We derive formulae for the amplification factor,  $A$ , as follows. For the disk/corona system  $A$ , defined by equation (10), can be rewritten in terms of the fraction of the energy released in the corona,  $f$  (Haardt & Maraschi 1991):

$$A_{\text{corona}} = 1 + \frac{f}{1 - f[1 - (1 - a)\eta]}. \quad (12)$$

To obtain the amplification factor in the hot inner flow,  $A_{\text{inner}}$ , we substitute the  $L_{\text{diss}}$  specified by equation (3) and the  $L_{\text{soft}}$  given by equation (6) into the equation (10).

### 2.3. Efficient, hot, spherical flow

In the simplest version, we assume that the hot inner flow efficiency is comparable to the disk efficiency, i.e.,  $\delta = 1$  in equation (3), and that the hot plasma forms a sphere with a radius  $r_{\text{tr}}$ .

The model parameters are

1. the mass of the black hole,  $M$ ;
2. the accretion rate,  $\dot{m}$ ;



3. the fraction of gravitational energy dissipated in the corona,  $f$ , (assumed constant with radius);
4. the transition radius,  $r_{\text{tr}}$ , at which the accretion disk evaporates to the spherical inner flow; and
5. the plasma temperature,  $kT_e$  (same in both Compton components).

#### 2.4. Low efficiency, hot, semispherical flow

The hot plasma located within the truncation radius,  $r_{\text{tr}}$ , may form an advection dominated flow, which was found to be several times less efficient than the accretion through the optically thick disk (see review by Narayan, Mahadevan & Quataert 1998). Chiang (2002) inferred the radiative efficiency in the Seyfert galaxy NGC 7469 to be  $\sim 2\%$ – $3\%$ . Thus, we also consider a case with  $\delta < 1$ . In our computations we assume  $\delta = 0.12$ , which corresponds to 1% accretion efficiency. In addition to the parameters listed in Section 2.3, we have now also the accretion efficiency correction,  $\delta$ .

In both cases (efficient and low efficiency inner flow), we check the possibility that the inner flow is flattened, i.e., the shape of the plasma within  $r_{\text{tr}}$  is ellipsoidal instead of spheroidal. Flattened, disk-like distribution of Comptonizing plasma was suggested by Chiang (2002) to explain spectra of the Seyfert galaxy NGC 3516. This modification adds the semi-minor axis of ellipsoidal flow,  $r_s < r_{\text{tr}}$ , to the list of model parameters.

The basic quantities that define the geometry in our approach are  $L_{\text{diss}}$  and  $L_{\text{soft}}$ . Allowing for  $\delta < 1$  affects both  $L_{\text{diss}}$  and  $L_{\text{soft}}$ , since  $L_{\text{soft}}$  depends on  $L_{\text{diss}}$  through  $F_{\text{soft}}$ ; see equations (5) and (4). Considering a flattened shape of the inner flow affects only  $L_{\text{soft}}$ , i.e. the soft flux intercepted by the inner flow.

### 3. Results

Based on the computed model spectra, we calculate spectral characteristics, such as the X-ray loudness,  $\alpha_{\text{ox}}$ , the X-ray photon index,  $\Gamma$ , and the optical/UV luminosity,  $l_{\text{UV}} \equiv \log(\nu L_\nu)$  at 2500 Å in the rest frame. Then we explore the model parameter space to find theoretical parameters compatible with the observed values of  $\alpha_{\text{ox}}$ ,  $\Gamma$ , and  $l$  in high- $z$  RQQs.

Figure 2 illustrates the sensitivity of the model spectrum to different model parameters. As expected, the bolometric luminosity depends on the accretion rate, with almost no change

in  $\alpha_{\text{ox}}$  and  $\Gamma$  (Fig. 2b). The most dramatic spectral change is due to variations in the truncation radius,  $r_{\text{tr}}$  (Fig. 2c), the electron temperature (which physically depends on the rate of cooling by soft photons; Fig. 2d), and the radiation efficiency of the central sphere,  $\delta$  (Fig. 2f).

Below, we discuss in detail the results with respect to the data of high-redshift RQQs. In particular, we search for values of the theoretical model parameters that give  $\Gamma < 2.3$  and  $1.5 < \alpha_{\text{ox}} < 1.8$ . Such a choice is motivated by the  $3\sigma$  confidence intervals of  $\Gamma$  given by V03 ( $1.7 \leq \Gamma \leq 2.3$ ), the results of Vignali et al. (2003b;  $\Gamma = 1.86^{+0.41}_{-0.37}$ ), and the B03 sample, with a mean photon index of  $\Gamma = 1.50 \pm 0.15$  (the error represents the 90% confidence interval). We choose the value of  $\alpha_{\text{ox},\text{min}} = 1.5$  for the lower limit, motivated by the value within the  $3\sigma$  confidence interval found for RQQs in the Bright Quasar Survey (see Brandt et al. 2002a and references therein). The upper limit of  $\alpha_{\text{ox},\text{max}} = 1.8$  was chosen on the basis of the samples of B03, with  $\alpha_{\text{ox}} = 1.71 \pm 0.02$  (the contributions to the error of  $\alpha_{\text{ox}}$  come only from errors of the X-ray photon index and the normalization of the power law fit to the data; in addition, the 2 keV flux in the source frame was calculated from the 1 keV flux in the observer frame, assuming the photon indices found from fits, not the value of 2.2 as assumed in B03), and V03, with  $\alpha_{\text{ox}} = 1.77 \pm 0.03$  (we cite the value of  $\alpha_{\text{ox}}$  corrected by the authors in a subsequent paper, Vignali et al. 2003b).

### 3.1. Efficient, Hot, Spherical Flow

The rest frame ultraviolet luminosity,  $l_{\text{UV}} \equiv \log \nu L_{\nu}$  at  $\nu = c/\lambda_{2500\text{\AA}}^{\circ}$ , depends on all model parameters except the plasma temperature,  $kT_e$ . For a black hole mass of the order of  $10^{10} M_{\odot}$ , the luminosity  $l_{\text{UV}} \sim 46.0\text{--}47.0$  can be obtained for any considered accretion rate if the corona above the truncated disk dissipates no more than about 10% of the gravitational potential energy, and the remaining  $\sim 90\%$  is dissipated in the disk (see Figure 3a). If the corona dissipates most of the energy, the UV bump becomes less pronounced, and the most luminous objects (with  $l_{\text{UV}} \gtrsim 47.0$ ) cannot be explained even with Eddington accretion rates unless the black hole mass is higher than  $10^{10} M_{\odot}$ .

Neither the X-ray slope,  $\Gamma$ , nor the X-ray loudness,  $\alpha_{\text{ox}}$ , depends on the accretion rate for a given truncation radius and fraction of energy dissipated in the corona (see Figure 2b). The change in the accretion rate influences only the normalization of the spectrum.

The X-ray photon index,  $\Gamma$ , depends on the strength of the corona,  $f$ , and the disk

truncation radius,  $r_{\text{tr}}$  (Fig. 2a and Fig. 2c). The strength of the corona needs to be fixed at  $\sim 10\%$  in order to match the observed optical/UV luminosity (as stated above), so the only parameter that determines  $\Gamma$  is the disk truncation radius,  $r_{\text{tr}}$ . If the truncation radius increases, the amplification factor of the hot inner flow,  $A_{\text{inner}}$ , increases, and a harder X-ray spectrum is produced. For  $4R_S < r_{\text{tr}} < 100R_S$ , the model gives an X-ray photon index ranging from  $\sim 2.3$  to  $\sim 1.6$ .

The X-ray loudness,  $\alpha_{\text{ox}}$ , depends on the strength of the corona above the disk,  $f$ , the truncation radius,  $r_{\text{tr}}$ , and the plasma temperature,  $kT_e$ . The strength of the corona,  $f$ , is constrained by the optical/UV luminosity. An increase in the disk truncation radius,  $r_{\text{tr}}$ , causes the X-ray loudness to decrease. This is because an accretion disk truncated farther away from the black hole produces a less pronounced optical/UV bump, and  $l_{\text{UV}}$  decreases. Simultaneously, the X-ray spectrum hardens (as described above), and a higher 2 keV flux is produced (see Figure 2c).

Variations of the electron temperature influence significantly the X-ray loudness,  $\alpha_{\text{ox}}$ , but do not influence the X-ray slope,  $\Gamma$  (Fig.2d). The maximum value of the X-ray loudness for a temperature of 150 keV is about 1.7. For a higher temperature,  $kT_e = 500$  keV, the maximum X-ray loudness,  $\alpha_{\text{ox,max}}$ , could be as high as  $\sim 2.2$ .

The lack of the dependence of the X-ray slope on the plasma temperature follows from the fact that in the model  $\Gamma$  is determined by the amplification factor; i.e., the X-ray slope is only geometry dependent. The sensitivity of the X-ray loudness to the plasma temperature can be explained by the fact that in thermal plasmas spectral characteristics, such as the X-ray photon index, the optical depth, and the electron temperature, are not independent. An increase in the electron temperature is compensated for by a decrease in the optical depth, resulting in approximately the same X-ray slope. The higher electron temperature implies the higher energy of the spectral cut-off. The total energy must, however, be conserved. Therefore, the normalization of the Comptonized component drops, resulting in the X-ray quieter spectra. Plasma temperature variations only weakly influence  $l_{\text{UV}}$ , through the dependence on the amount of the soft radiation that escapes the plasma without being Comptonized on  $kT_e$  (see Equation (11)). However, this effect is not significant enough to influence the results.

Figure 4 summarizes the above results and shows two observationally interesting regions,  $1.5 \leq \alpha_{\text{ox}} \leq 1.8$  and  $1.7 \leq \Gamma \leq 2.3$ , in the *truncation radius–accretion rate* plane. The computations were performed for two electron temperatures,  $kT_e = 150$  and 500 keV, and two values of the fraction of energy dissipated in the corona,  $f = 0.1$  and  $f = 0.6$ . For an electron temperature of 150 keV and  $f = 0.1$ , the two regions overlap if the transition radius is of the order of several  $R_S$ . The spectra are relatively soft and X-ray loud, with  $\Gamma \sim 2.0$ – $2.3$

and  $\alpha_{\text{ox}} \sim 1.5 - 1.7$  (Figure 4a). For higher electron temperatures, the overlapping region exists at higher truncation radii ( $r_{\text{tr}} \sim 7 - 15 R_{\text{S}}$  for  $kT_e = 500$  keV). In addition, harder ( $\Gamma < 2.0$ ) and X-ray quieter ( $\alpha_{\text{ox}} \sim 1.7-1.8$ ) spectra can be obtained (Figure 4b). A stronger corona ( $f = 0.6$ ) requires a higher electron temperature ( $kT_e \gtrsim 200$  keV) to produce spectra with  $\Gamma \sim 2.0 - 2.3$  and  $\alpha_{\text{ox}} \sim 1.5 - 1.7$ . For  $kT_e \gtrsim 400$  keV, the model additionally gives spectra with  $\alpha_{\text{ox}} \sim 1.7 - 1.8$  and  $\Gamma \sim 2.0 - 2.3$ , or  $\alpha_{\text{ox}} \sim 1.5 - 1.7$  and  $\Gamma \sim 1.7 - 2.0$  (Figure 4c). However, in case of  $f = 0.6$ , the optical/UV luminosity is  $l_{\text{UV}} \leq 46.2$ .

### 3.2. Low-Efficiency, Hot, Semispherical Flow

We compute  $\alpha_{\text{ox}}$ ,  $\Gamma$ , and  $l_{\text{UV}}$  in the low efficiency hot inner flow model (Section 2.4). All the spectral trends with the strength of the corona, the accretion rate, the truncation radius, and the electron temperature are qualitatively the same as for the high efficiency hot flow. As in Section 3.1, a weak corona above the disk is required in order to fit the optical/UV luminosity. The dependence of  $l_{\text{UV}}$  on the truncation radius and the accretion rate for  $f = 0.1$  is shown in Figure 3b.

Figure 2f shows dramatic changes in the X-ray slope,  $\Gamma$ , and X-ray loudness,  $\alpha_{\text{ox}}$ , with reduced efficiency of the central hot flow. For a given truncation radius,  $r_{\text{tr}}$ , less heat is being supplied to the electrons (some of the energy is advected); i.e., the total luminosity of the hot flow decreases,  $L_{\text{diss}}(\delta < 1) < L_{\text{diss}}(\delta = 1)$ . The soft disk luminosity intercepted by the hot flow,  $L_{\text{soft}}$ , also decreases, because it depends on the hot flow luminosity through  $F_{\text{inc}}$  (see equations (5) and (4)). However,  $L_{\text{diss}}$  decreases faster than  $L_{\text{soft}}$ , since the latter contains contribution from the viscous dissipation in the outer disk. Thus, lowering the hot flow efficiency causes a decrease in the amplification factor of the hot flow,  $A_{\text{inner}}$ , and leads to a softer X-ray spectrum. In addition, decreasing  $L_{\text{soft}}$  lowers the normalization of the soft input spectrum for Comptonization in the hot flow, which results in a lower normalization of the X-ray continuum and X-ray quieter spectra. This can be clearly seen in Figure 2f for the plasma temperature of 500 keV.

To summarize, for a given truncation radius,  $r_{\text{tr}}$ , lowering the efficiency of the hot inner flow leads to a softer X-ray slope and X-ray quieter spectra. This result is illustrated in Figure 5. To produce spectra with the same  $\Gamma$  and  $\alpha_{\text{ox}}$  as in the case of the efficient flow (compare Figure 4), a sphere with a larger radius is required. As in Section 3.1, a plasma temperature higher than  $\sim 150$  keV and a fraction of energy dissipated in the corona smaller than  $\sim 10\%$  are implied by the data. However, the transition radius now falls into the range of  $\sim 10 - 70 R_{\text{S}}$ , depending on the strength of the corona, the plasma temperature, and the

accretion rate. The hardest,  $\Gamma \sim 1.7 - 2.0$ , and X-ray quietest,  $\alpha_{\text{ox}} \sim 1.7 - 1.8$ , spectra can be obtained for higher electron temperatures. Figure 5b shows the case of  $kT_e = 500$  keV with the solution for  $r_{\text{tr}} \sim 30 - 40 R_S$ .

In the second modification to the efficient flow, we allow for a flattening of the central sphere, e.g., an ellipsoidal flow. The amplification factor now depends strongly not only on  $r_{\text{tr}}$ , but also on the semi-minor axis of the ellipsoidal flow,  $r_s$ , and on the ratio  $r_s/r_{\text{tr}}$ . For a given transition radius there exists the following trend: the smaller the  $r_s$ , the harder the spectra (see Figure 2e). This is because the luminosity,  $L_{\text{soft}}$ , drops, resulting in an increase of the hot flow amplification factor,  $A_{\text{inner}}$  ( $L_{\text{diss}}$  remains constant). This geometry may produce spectra as hard as  $\Gamma = 1.5$ , but with  $\alpha_{\text{ox}}$  significantly smaller than that observed in high- $z$  RQQs if the hot inner flow is efficient,  $\delta = 1$  (Section 2.3). If the radiative efficiency is reduced,  $\delta < 1$  (Section 2.4), allowing for ellipsoidal central flow results in a shift of the regions indicated in Figure 5 toward slightly lower transition radii (i.e., it is an intermediate case between efficient spherical inner flow and efficient flattened inner flow). Thus, we consider  $r_{\text{tr}} \sim 40 R_S$  to be an upper limit of the truncation radius in the model that allows us to obtain the X-ray quietest spectra with  $\alpha_{\text{ox}} \sim 1.7 - 1.8$ .

We note that the objects with very hard photon indices,  $\Gamma < 1.5$ , cannot be explained by the model, because the X-ray loudness of such spectra is always lower than  $\alpha_{\text{ox}} = 1.5-1.8$ .

#### 4. Application to the data

We apply the model to eight high redshift RQQ from the BO3 sample. We choose only the seven sources with observed photon index  $\Gamma > 1.5$ . We also include the highest redshift quasar, at  $z=6.28$ . We do not perform a formal  $\chi^2$  fitting to determine the best-fit parameters and their confidence limits, but rather demonstrate the parameter values that approximately reproduce the spectra. With the available data the results are not unique, and a number of solutions are possible. The computed spectra are shown in Figures 6 and 7. The fit parameters are listed in Tables 1 (efficient inner flow) and 2 (low efficiency inner flow). The objects were observed by *Chandra* in the 0.3–6.5 keV range. The 1450 Å rest frame points were taken from the literature, as described in detail in B03. The ratio of the optical/UV and X-ray fluxes is characterized by the X-ray loudness. In the case of high- $z$  quasars, the 2500 Å flux used to calculate  $\alpha_{\text{ox}}$  must be extrapolated from the 1450 Å flux known from observations, which involves a knowledge of the optical/UV spectral index ( $f_\nu \sim \nu^{\alpha_{\text{UV}}}$ ). To derive general properties of a theoretical model or an observational sample, a mean value suggested by observations can be used (as in Section 3 or in B03, where  $\alpha_{\text{UV}} = -0.3$  was

adopted; Kuhn et al. 2001)). However, it does not apply to modeling the spectra of particular objects. Thus, in this section we use the flux at 1450 Å to normalize the spectrum, and we list values of the spectral index between rest frame 1450 and 2500 Å,  $\alpha_{\text{UV}}$ , and the X-ray loudness,  $\alpha_{\text{ox}}$ , computed from the model spectra in Tables 1 and 2. The optical and X-ray observations were not simultaneous. However, Giveon et al. (1999) argue that the optical variability anti-correlates with the luminosity of AGNs. Given that the high- $z$  RQQs are very luminous objects, one would expect optical variability at a relatively low level.

Matching the observed optical/UV luminosity requires weak coronae above the accretion disk, dissipating no more than  $\sim 10\%$  of the gravitational potential energy. In addition, high masses of the central black holes should be considered,  $M \sim (0.5 - 1.4) \times 10^{10} M_{\odot}$ . Our modeling of BRI0103+0032 illustrates the following trend: an increase of the black hole mass (with the X-ray slope kept constant) forces the accretion rate to decrease in order to fit the optical/UV luminosity. In addition, the electron temperature drops (the plasma optical depth increases) to match the X-ray emission.

For the radiatively efficient spherical inner flow (Section 2.3;  $\delta = 1$  and  $r_{\text{s}} = r_{\text{tr}}$ ), the truncation radius of the accretion disk is typically 5–11  $R_{\text{S}}$ . This is constrained mainly by the observed X-ray slope. In general, the electron temperatures of  $\sim 108$ –500 keV are required in order to match the observed X-ray loudness. The X-ray quietest objects in our sample ( $\alpha_{\text{ox}} \sim 1.7 - 1.8$ ; PSS1057+4555, SDS1030+0524, and SDS1204-0021) require very low optical depth of the plasma ( $\tau < 0.05$ ), which brings the temperature to unrealistically high values of 700–1400 keV. Thus, models with  $\delta = 1$  are not acceptable, at least for PSS1057+4555, SDS1030+0524, and SDS1204-0021.

Considering a flattened hot inner flow allows for slightly lower electron temperatures. However, in the case of objects with  $\alpha_{\text{ox}} \sim 1.7$ –1.8, the electron temperature is still high, ranging from 410 to 800 keV. In the case of the two objects with  $\Gamma > 2.3$ , there is no need to introduce this modification, since the flattening of the hot flow would cause the hardening of the spectrum. These soft objects can be modeled with a very small hot inner flow (with  $r_{\text{tr}} \sim 5 R_{\text{S}}$ ) or even with a standard plane-parallel configuration in which the accretion disk covered with a hot corona extends down to the last stable orbit,  $r_{\text{in}}$  (in Table 1, fits with  $r_{\text{tr}} = r_{\text{s}} = r_{\text{in}}$ ). In addition, the corona may be stronger and can dissipate up to 70% of the energy (see fits for BRI1033-0327 and PSS1317+3531 in Table 1).

Assuming the low efficiency spherical flow (Section 2.4;  $\delta < 1$ ,  $r_{\text{tr}} = r_{\text{s}}$ ) results in an increase of the disk truncation radius needed to fit the observed X-ray slope. Now  $r_{\text{tr}} \sim 9 - 35 R_{\text{S}}$  (see Table 2). The electron temperature needed to match the observed X-ray loudness is  $kT_{\text{e}} \sim 90$ –345 keV. However, the objects with the hardest X-ray spectra (SDS1030+0524 and SDS1204-0021) cannot be modelled using low efficiency spherical flow

geometry. Reproducing their X-ray slope (within a  $1\sigma$  confidence interval) requires the disk to be truncated at  $60 - 80 R_S$ . With this large an  $r_{\text{tr}}$ , the black hole mass would have to be larger than  $2 \times 10^{10} M_\odot$  in order to fit the optical/UV luminosity, even assuming accretion at the Eddington rate. Even then the fit is not acceptable, because of the optical/UV spectral index (we discuss this issue in more detail below).

We also perform fits in which we allow for both low efficiency and flattening of the hot inner flow. In this approach, all the objects with  $\Gamma < 2.3$  can be modeled. The disk truncation radius is  $r_{\text{tr}} \sim 11-20 R_S$ , the semi-minor axis of the inner flow is  $r_s \sim 4-10 R_S$ , and the electron temperature ranges from  $\sim 195$  to  $\sim 500$  keV.

The model covers a wide range of the optical/UV spectral index. For the efficient inner flow, we get  $-0.6 < \alpha_{\text{UV}} < -0.3$  and for low efficiency inner flow,  $-1.5 < \alpha_{\text{UV}} < -0.3$ . These values are in agreement with observations that suggest a significant spread in  $\alpha_{\text{UV}}$ ; e.g., Fan et al. (2001) derive  $\alpha_{\text{UV}} = -0.79 \pm 0.34$  ( $1\sigma$ ), and Pentericci et al. (2003) report on  $\alpha_{\text{UV}} = -0.57 \pm 0.33$  ( $1\sigma$ ) for high- $z$  quasars ( $3.6 < z < 5$ ). Knowing the exact value of  $\alpha_{\text{UV}}$  for individual sources would reduce the number of model parameters and make the fitting procedure unique.

We stress that the results for the plasma temperature and optical depth come from the constraint placed by the ratio of optical/UV to X-ray emission. The values of X-ray loudness we obtain from fits differ by up to 16% from those given by B03. This difference comes from the adoption of  $\alpha_{\text{UV}} = -0.3$  and  $\Gamma = 2.2$  by B03 when calculating  $\alpha_{\text{ox}}$ .

Our modeling implies a rather high accretion rate,  $\dot{M} \sim 0.2-1.4 \dot{M}_{\text{Edd}}$ . This would suggest that the high- $z$  RQQs may correspond to high or very high states of black hole binaries (see the comparison of AGN and XRB luminosity states in Czerny 2003). However, the accretion disk in the high or very high state of an XRB is expected to extend to the last stable orbit (e.g., Esin, McClintock, & Narayan 1997).

## 5. Discussion

We have computed optical/UV/X-ray spectra from a two-component accretion flow in the geometry with a hot, semispherical inner flow enclosed by a truncated accretion disk covered with a hot corona. We assumed that the soft disk blackbody-like radiation was Comptonized in the hot plasma and that the electron energy distribution in the hot plasma was thermal. We investigated the values of model parameters for which the model can account for spectra observed in high-redshift RQQs. Such spectra can be characterized by



three observables: (1) the luminosity at 1450 Å in the rest frame of the source,  $l_{\text{UV}} \equiv \log(\nu L_\nu) \gtrsim 46.0\text{--}47.0$ , (2) the X-ray loudness,  $\alpha_{\text{ox}} \sim 1.5\text{--}1.8$ , and (3) the X-ray photon index,  $\Gamma \sim 1.7\text{--}2.3$ . Finally, we applied the model to the RQQ data of B03.

The high luminosities of objects in our sample require not only rather large black hole masses,  $\sim 10^{10} M_\odot$ , but also high accretion rates, above  $0.2 \dot{M}_{\text{Edd}}$ .

We found that some objects require the radiative efficiency of the hot inner flow to be reduced compared to that of the standard Keplerian disk. A significant fraction of the energy is then advected inwards, rather than radiated (i.e., an ADAF-like flow). The hardest ( $\Gamma \leq 2.0$ ) and X-ray quietest ( $\alpha_{\text{ox}} \sim 1.7\text{--}1.8$ ) spectra require a truncation radius up to  $r_{\text{tr}} \sim 30\text{--}40 R_{\text{S}}$  if the inner flow is spherical. If the inner flow is additionally flattened, the truncation radius is smaller, yielding  $\sim 15\text{--}30 R_{\text{S}}$ .

These values of the truncation radius are comparable to those obtained by Janiuk et al. (2004), who studied a time evolution of unstable accretion disks with possible disk evaporation. Janiuk et al. considered the effects of the MHD turbulence on the viscosity during the evolution of the thermal-viscous ionization instability in the standard  $\alpha$ -accretion disks, in order to explain intermittent activity in AGNs. They considered the possibility of accretion through a truncated disk whose inner part is evaporated to an ADAF-like flow. They found that the evaporation is also important during the outbursts, even at relatively high accretion rates of  $0.1 \dot{M}_{\text{Edd}}$ . The disk then truncates at  $\sim 25 R_{\text{S}}$  (for a black hole mass of  $10^8 M_\odot$  and viscosity parameter  $\alpha = 0.1$ ). We note, however, that their value for the disk truncation radius depends strongly on the adopted value of the viscosity parameter.

We were not able to model objects with very hard X-ray spectra ( $\Gamma = 0.33\text{--}1.44$  in the B03 sample). Such hard spectra can be produced within the model for the accretion disk truncated far away from the black hole ( $r_{\text{tr}} \gg 10^2 R_{\text{S}}$ ). However, the optical/UV part of the spectrum is then suppressed and the model  $\alpha_{\text{ox}}$  value is much smaller than that observed.

The truncation radius can, in principle, be tested using the X-ray reflection component. In the considered geometry, most of the X-ray reflection comes from disk radii close to  $r_{\text{tr}}$ , so the sharp spectral features (Fe K $\alpha$  line and edge) should be broadened by the relativistic effects (Fabian et al. 1989; Laor 1991). The amount of reflection is given by the amplitude of the reflected component,  $R$ . In our approach, the accretion disk may reflect hard X-rays emitted by both the hot corona and the hot inner flow. The amplitude of reflection is thus given in our model by

$$R = \frac{L_{\text{inc}}}{L_{\text{hard}}}, \quad (13)$$

where  $L_{\text{inc}}$  is the luminosity emitted by the hot plasma (hot inner flow + hot corona) toward the accretion disk and  $L_{\text{hard}}$  is the total luminosity of the hot plasma (hot inner flow + hot

corona) as seen by a distant observer, i.e.,

$$L_{\text{inc}} = L_{\text{sphere,inc}} + L_{\text{corona,inc}} = 2\pi \int_{r_{\text{tr}}}^{\infty} r F_{\text{inc}}(r) dr + 2\pi \int_{r_{\text{tr}}}^{\infty} r F_{\text{visc}}(r) \eta f dr \quad (14)$$

(we take  $2\pi$ , since we consider a top view scenario in which the observer sees just one surface of the disk), and

$$L_{\text{hard}} = L_{\text{diss}} + 2\pi \int_{r_{\text{tr}}}^{\infty} r F_{\text{visc}}(r) (1 - \eta) f dr. \quad (15)$$

The reflection amplitude of only the coronal radiation yields  $R = 1$ , if one assumes isotropic Comptonization with  $\eta = 0.5$  (Haardt & Maraschi 1991). However, in our geometry the dominant contribution comes from the reflection of the inner flow radiation by the disk. Thus, the typical values of the amplitude of reflection are  $R = 0.2\text{--}0.6$  (the efficient, spherical inner flow) and  $R = 0.15\text{--}0.35$  (low-efficiency, semispherical inner flow). The lower value of the reflection amplitude in the case of the low-efficiency, semispherical inner flow is caused by the higher value of the disk truncation radius needed to fit the data (see Table 2). The higher truncation radius (i.e., the accretion disk is truncated farther away from the black hole) means a smaller contribution from the reflection of coronal radiation. We note that if the  $R - \Gamma$  correlation observed in XRBs and Seyfert galaxies (Zdziarski, Lubiński, Smith 1999) also holds for high- $z$  RQQs, this model may account for it. In the case of objects with high accretion rates, the reflecting material will be highly ionized. As a result, the reflected component at energies smaller than the fluorescent iron line energy will be flatter, as compared to neutral reflection. Given the small amplitude of the reflected component calculated above, we estimate that the change of the X-ray slope due to reflection will be not bigger than 0.1–0.2, which is well within observational errors. Tests involving studies of the reflected continuum and iron fluorescence line require X-ray data of good quality, with the uncertainties not exceeding 1%, which may be available in the future observations with, for example, *ASTRO-E2* and the *Constellation-X* mission.

Results of our modeling imply that the temperature of Comptonizing plasma should be rather high, up to 500 keV. This constraint comes from the required low optical depth of the Comptonizing plasma needed to reproduce the relatively low normalization of hard X-rays compared to that of the disk component (i.e., the high value of  $\alpha_{\text{ox}}$ ). In Figure 8, we present the range of the amplification factor that we obtain for the Comptonization in the efficient, hot, spherical inner flow ( $A = 2.5\text{--}60$ , lower axis) and the corresponding range of the optical depths ( $\tau = 0.3\text{--}1.0$ ; upper axis) for the electron temperature 150 keV. Similar dependencies are shown for the Comptonization in the corona ( $A = 1.0\text{--}3.5$ ;  $\tau = 0.05\text{--}0.37$ ). Obviously, the higher the electron temperature, the lower the optical depth, because the X-ray spectral slope is fixed by the data.

Fits to the spectra of accreting black hole XRBs in the hard state and local Seyfert galaxies give electron temperatures of 50–150 keV and optical depths of the order of  $\tau \sim 1$  (Gierliński et al. 1997; Zdziarski et al. 1998; Zdziarski, Poutanen & Johnson 2000; Done et al. 2000). In particular, Zdziarski et al. (2000) analyzed the average spectrum of 17 radio quiet Seyfert 1 galaxies in the 50–500 keV range observed with OSSE. They chose the spherical geometry with an input of soft photons at the temperature of 10 eV in the center of the sphere. They used the `compps` model in the XSPEC package to fit the Comptonized continuum together with the reflection feature. Thus, the high energy cutoff in the model spectrum, which determines the plasma temperature as a physical parameter, was directly constrained by the data points. Their derived plasma temperatures for Seyfert galaxies were much lower than the temperatures required for high redshift quasars in our modelling.

On the other hand, Chiang (2002) and Chiang & Blaes (2003) performed analysis of three Seyfert galaxies that was very similar to the analysis in the present paper. By fitting the spectra including both the optical/UV and the 2–20 keV continuum, they also obtained rather high plasma temperatures (sometimes above 500 keV) and low optical depths. The difference between their approach and the approach of Zdziarski, Poutanen & Johnson (2000) was modeling the X-ray data together with optical/UV data. In addition, Chiang (2002) and Chiang & Blaes (2003) attempted to additionally constrain their model by inferring black hole masses and disk truncation radii from other observations (reverberation mapping, width of the Fe K $\alpha$  line, etc.). They did not use data above 30 keV, so the hard X-ray cutoff was a free parameter in their model, as it was in ours.

To qualitatively compare high- and low- $z$  objects, we perform exemplary fits to the Seyfert galaxy NGC 7469 (analyzed by Chiang 2002) and the low- $z$  ( $z=0.206$ ) quasar PG 0947+396 from a sample described in Laor et al. (1997). For NGC 7469 we obtain a good fit for  $kT_e = 110$  keV and  $\tau_s = 0.8$  (in agreement with findings of Zdziarski et al. 2000), a truncation radius of  $r_{\text{tr}} = 27 R_S$ , an accretion rate of 0.17 times the Eddington rate, and a mass of  $5 \times 10^7 M_\odot$ . The inner flow efficiency is low, comparable to that of Chiang (2002). In the case of PG 0947+396, we require the accretion disk to extend to the last stable orbit, the corona to dissipate 40% of the energy, the plasma temperature  $kT_e$  to be 230 keV, and the optical depth  $\tau_c$  to be 0.1. The mass estimate is  $5 \times 10^8 M_\odot$ , and the accretion rate accounts for 0.7 times the Eddington rate. These results suggest that low- $z$  objects can be modeled with lower masses and different plasma parameters (lower temperatures and higher optical depths). However, a satisfactory comparison between low- and high- $z$  samples cannot be made at this stage. First, the X-ray data do not correspond to the same rest frame energies: 2–30 keV for high- $z$  quasars, 2–10 keV for NGC 7469 (Nandra 2000), and 0.3–2 keV for PG 0947+396 (Laor et al. 1997). Second, the low- $z$  objects require very detailed data analysis in the 0.3–10 keV X-ray range to model the soft X-ray excess, and above 10 keV to model

hard X-rays. In principle, our model is able to explain the soft excess in terms of two Comptonizations, since it includes two Comptonizing media: a corona above the accretion disk and an inner flow, unlike, e.g., the models of Chiang (2002) and Chiang & Blaes (2003). However, in the recent paper of Gierliński & Done (2004), the authors model the 0.3–20 keV range with only one Comptonization component and a complex absorption feature and point out that the soft X-ray excess may be an artifact of such an absorption. The present data of high- $z$  quasars do not allow a determination of whether their rest-frame spectra show the soft X-ray excess or not, because the component is redshifted below the observable band. On the other hand, some absorption features may become important in the future, higher quality X-ray data.

Modeling broad-band quasar spectra including both accretion disk emission and the Comptonized hard X-rays provides a difficult theoretical challenge. Reproducing the relative normalization of the two main emission components requires rather detailed knowledge of the geometry and emission mechanisms and patterns. Moreover, the high accretion rate inferred from our modeling implies that the studied objects may correspond to high or very high states of galactic black hole binaries. In addition, the resulting high electron temperatures and low optical depths in the scenario with a thermal plasma may suggest that the Comptonization actually takes place in non-thermal or hybrid plasmas, as is seen in XRBs in their high state (i.e., Gierliński et al. 1999). Many detailed studies of XRBs reveal complex, multi-component spectra (see, e.g., Życki, Done & Smith 2001; Wilson & Done 2001; Gierliński & Done 2003). The spectra contain not only simple disk emission with a hard Comptonized component, but also additional Comptonization of the disk emission, modification due to X-ray irradiation of the external regions of the disk, and the reprocessed component, usually ionized and relativistically smeared. These additional components are also detected in AGN spectra (e.g., PG 1211+143; Janiuk, Czerny & Madejski 2001), and will surely have to be incorporated into future models (e.g., Czerny et al. 2003).

## 6. Conclusions

In this paper we explored a parameter space of the semi-spherical accretion models applicable to high- $z$  RQQs. Our results show the following:

1. The observed optical/UV luminosity suggests that high redshift quasars host supermassive black holes with masses of the order of  $10^{10} M_{\odot}$ . The modeling results in accretion rates higher than  $\sim 0.2$  times the Eddington rate.

2. The high accretion rates may suggest similarity between high- $z$  RQQs and XRBs in the high or very high state. If high- $z$  RQQs correspond to high or very high states of X-ray binaries, the high values of plasma temperature (up to 500 keV) and low optical depths might suggest instead that Comptonization takes place in a non-thermal or hybrid plasma.
3. The observed X-ray loudness puts strong constraints on the modeled plasma temperature and optical depth. *Chandra* or *XMM-Newton* observations with better S/N are needed to give tighter constraints on the X-ray slope. Future mission (such as *Constellation-X*) can provide information about the high-energy cut-off and the reflected component that is necessary to uniquely determine geometry of the accretion flow.
4. Precise observations constraining the optical/UV spectral index for individual sources would help to reduce the number of model parameters and perform more accurate fits. However, the intrinsic reddening of the quasar spectrum is the main observational uncertainty in this spectral region.
5. With the present data, a number of theoretical descriptions are possible. In Paper II, we focus on another interesting possibility, in which the accretion disk extends to the last stable orbit and the hot Comptonizing corona is formed by clouds above the disk (the “patchy” corona geometry).

We thank Martin Elvis, Paul Green, Jill Bechtold, and Jim Chiang for many discussions. We also thank the anonymous referee for detailed reading of the manuscript and helpful comments. This research is funded in part by NASA contract NAS8-39073. Partial support for this work was provided by the National Aeronautics and Space Administration through *Chandra* Awards Number GO1-2117B and GO2-3148A, issued by the *Chandra* X-Ray Center, which is operated by the Smithsonian Astrophysical Observatory for and on behalf of NASA, under contract NAS8-39073. M.A.S. and P.T.Ž. were partially supported by the grant PBZ-KBN-054/P03/2001 and KBN project number 2P03D00322. M.A.S. acknowledges support from the Smithsonian Institution Pre-doctoral Fellowship program.

## A. Appendix

For completeness, we give here expressions for  $g(r)$ ,  $\alpha_{\max}$ ,  $\phi_{\max}$ , and  $l(r, \alpha, \phi, r_s)$  (see Chiang 2002):

$$g(r) = 2 \int_0^{\alpha_{\max}} \phi_{\max}(\alpha, r) \sin \alpha \cos \alpha d\alpha,$$

$$\alpha_{\max} = \tan^{-1} \left( \frac{r_s}{(r^2 - r_{\text{tr}}^2)^{1/2}} \right),$$

$$\phi_{\max} = \cos^{-1} \left[ \frac{[(r^2 - r_{\text{tr}}^2)(r_s^2 + \tan^2 \alpha)]^{1/2}}{rr_s} \right],$$

$$l = \frac{2r_s [(r_s^2 + \tan^2 \alpha) - r^2(\tan^2 \alpha + r_s^2 \sin^2 \phi)]^{1/2}}{\cos \alpha (r_s^2 + \tan^2 \alpha)}.$$

## REFERENCES

- Band, D. L. & Malkan, M. A. 1988, BAAS, 20, 1073
- Bechtold, J. et al. 1994a, AJ, 108, 374
- Bechtold, J. et al. 1994b, AJ, 108, 759
- Bechtold, J. et al. 2003, ApJ, 588, 119 (B03)
- Becker, R. H. et al. 2001, AJ, 122, 2850
- Beloborodov, A. M. 1999a, ApJ, 510, L123
- Beloborodov, A. M. 1999b, ASP Conf. Ser. 161: High Energy Processes in Accreting Black Holes, 295
- Brandt, W. N., Vignali, C., Fan, X., Kaspi, S., & Schneider, D. P. 2002a, X-ray Spectroscopy of AGN with Chandra and XMM-Newton, 235
- Brandt, W. N. et al. 2002b, ApJ, 569, L5
- Cappi, M., Matsuoka, M., Comastri, A., Brinkmann, W., Elvis, M., Palumbo, G. G. C., & Vignali, C. 1997, ApJ, 478, 492
- Chiang, J. 2002, ApJ, 572, 79
- Chiang, J. & Blaes, O. 2003, ApJ, 586, 97
- Collin-Souffrin, S., Czerny, B., Dumont, A.-M., & Życki, P. T. 1996, A&A, 314, 393
- Coppi, P. S. 1999, ASP Conf. Ser. 161: High Energy Processes in Accreting Black Holes, 375
- Czerny, B. & Elvis, M. 1987, ApJ, 321, 305

- Czerny, B., Nikolajuk, M., Różańska, A., Dumont, A.-M., Loska, Z., & Zychki, P. T. 2003, *A&A*, 412, 317
- Czerny, B. 2003, *ASP Conf. Ser.* 290: Active Galactic Nuclei: From Central Engine to Host Galaxy, 59
- Done, C., Madejski, G. M., Życki, P. T. 2000, *ApJ*, 536, 213
- Done, C. 2001, *ASP Conf. Ser.* 251: New Century of X-ray Astronomy, 102
- Esin, A. A., McClintock, J. E., & Narayan, R. 1997, *ApJ*, 489, 865
- Fabian, A. C., Rees, M. J., Stella, L., & White, N. E. 1989, *MNRAS*, 238, 729
- Fan, X. et al. 2001, *AJ*, 121, 31
- Fiore, F., Elvis, M., Siemiginowska, A., Wilkes, B. J., McDowell, J. C., & Mathur, S. 1995, *ApJ*, 449, 74
- Galeev, A. A., Rosner, R., & Vaiana, G. S. 1979, *ApJ*, 229, 318
- George, I. M. & Fabian, A. C. 1991, *MNRAS*, 249, 352
- Gierliński, M., Zdziarski, A. A., Done, C., Johnson, W. N., Ebisawa, K., Ueda, Y., Haardt, F., & Phlips, B. F. 1997, *MNRAS*, 288, 958
- Gierliński, M., Zdziarski, A. A., Poutanen, J., Coppi, P. S., Ebisawa, K., & Johnson, W. N. 1999, *MNRAS*, 309, 496
- Gierliński, M. & Done, C. 2004, *MNRAS*, 349, L7
- Giveon, U., Maoz, D., Kaspi, S., Netzer, H., & Smith, P. S. 1999, *MNRAS*, 306, 637
- Haardt, F. & Maraschi, L. 1991, *ApJ*, 380, L51
- Haardt, F. & Maraschi, L. 1993, *ApJ*, 413, 507
- Janiuk, A., Czerny, B., & Madejski, G. M. 2001, *ApJ*, 557, 408
- Janiuk, A., Czerny, B., Siemiginowska, A., & Szczerba, R. 2004, *ApJ*, 602, 595
- Koratkar, A. & Blaes, O. 1999, *PASP*, 111, 1
- Kuhn, O., Elvis, M., Bechtold, J., & Elston, R. 2001, *ApJS*, 136, 225
- Laor, A., Fiore, F., Elvis, M., Wilkes, B. J., & McDowell, J. C. 1997, *ApJ*, 477, 93



- Laor, A. 1991, *ApJ*, 376, 90
- Lawson, A. J. & Turner, M. J. L. 1997, *MNRAS*, 288, 920
- Lightman, A. P. & White, T. R. 1988, *ApJ*, 335, 57
- McClintock, J. E. & Remillard, R. A. 2003, astro-ph/0306213, to appear in *Compact Stellar X-ray Sources*, eds. W.H.G. Lewin and M. van der Klis
- Mineo, T. et al. 2000, *A&A*, 359, 471
- Mushotzky, R. F., Done, C., & Pounds, K. A. 1993, *ARA&A*, 31, 717
- Nandra, K., Le, T., George, I. M., Edelson, R. A., Mushotzky, R. F., Peterson, B. M., & Turner, T. J. 2000, *ApJ*, 544, 734
- Narayan, R., Mahadevan, R., & Quataert, E. 1998, *Theory of Black Hole Accretion Disks*, 148
- Nayakshin, S. 2000a, *ApJ*, 534, 718
- Nayakshin, S., Kazanas, D., & Kallman, T. R. 2000b, *ApJ*, 537, 833
- Page, K. L., Turner, M. J. L., Reeves, J. N., O'Brien, P. T., & Sembay, S. 2003, *MNRAS*, 338, 1004
- Pentericci, L. et al. 2003, *A&A*, 410, 75
- Poutanen, J., Krolik, J. H., & Ryde, F. 1997, *MNRAS*, 292, L21
- Reeves, J. N. & Turner, M. J. L. 2000, *MNRAS*, 316, 234
- Rózańska, A. & Czerny, B. 2000, *A&A*, 360, 1170
- Shakura, N. I. & Sunyaev, R. A. 1973, *A&A*, 24, 337
- Shapiro, S. L., Lightman, A. P., & Eardley, D. M. 1976, *ApJ*, 204, 187
- Shields, G. A. 1978, *Nature*, 272, 706
- Siebert, J., Matsuoka, M., Brinkmann, W., Cappi, M., Mihara, T., & Takahashi, T. 1996, *A&A*, 307, 8
- Siemiginowska, A., Kuhn, O., Elvis, M., Fiore, F., McDowell, J., & Wilkes, B. J. 1995, *ApJ*, 454, 77

- Sobolewska, M. A., Siemiginowska, A., & Życki, P. T. 2004, accepted for publication in ApJ (Paper II)
- Stern, B. E., Poutanen, J., Svensson, R., Sikora, M., & Begelman, M. C. 1995, ApJ, 449, L13
- Stern, D., Djorgovski, S. G., Perley, R. A., de Carvalho, R. R., & Wall, J. V. 2000, AJ, 119, 1526
- Sun, W. & Malkan, M. A. 1989, ApJ, 346, 68
- Tripp, T. M., Bechtold, J., & Green, R. F. 1994, ApJ, 433, 533
- Vignali, C., Brandt, W. N., Schneider, D. P., Garmire, G. P., & Kaspi, S. 2003a, AJ, 125, 418 (V03)
- Vignali, C. et al. 2003b, AJ, 125, 2876
- Wilson, C. D. & Done, C. 2001, MNRAS, 325, 167
- Worrall, D. M., Tananbaum, H., Giommi, P., & Zamorani, G. 1987, ApJ, 313, 596
- Zamorani, G. et al. 1981, ApJ, 245, 357
- Zdziarski, A. A., Lubiński, P., & Smith, D. A. 1999, MNRAS, 303, L11
- Zdziarski, A. A., Poutanen, J., Mikołajewska, J., Gierliński, M., Ebisawa, K., & Johnson, W. N. 1998, MNRAS, 301, 435
- Zdziarski, A. A., Poutanen, J., & Johnson, W. N. 2000, ApJ, 542, 703
- Życki, P. T. & Czerny, B. 1994, MNRAS, 266, 653
- Życki, P. T., Done, C., & Smith, D. A. 2001, MNRAS, 326, 1367

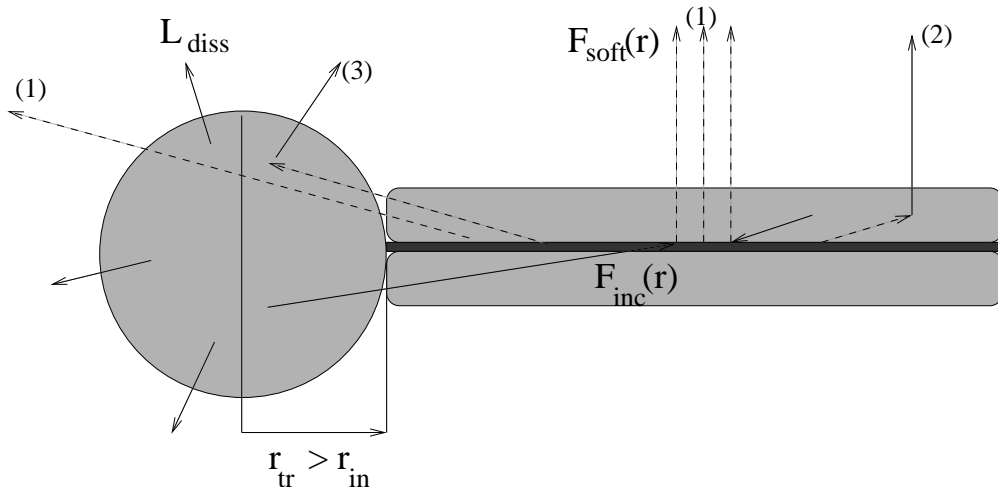


Fig. 1.— Hot inner flow geometry. The accretion disk evaporates at a radius  $r_{\text{tr}} > r_{\text{in}}$  and forms a hot, semispherical inner flow. The total luminosity of the hot inner flow is  $L_{\text{diss}}$ . The truncated disk is covered with a hot corona at radii  $r > r_{\text{tr}}$ . At each radius  $r > r_{\text{tr}}$ , three components contribute to the soft disk flux  $F_{\text{soft}}(r)$ : a viscous dissipation in the disk; reprocessing of the hard coronal radiation; and reprocessing of the hard radiation from the inner flow,  $F_{\text{inc}}(r)$ . The spectrum is composed of (1) the soft disk blackbody-like radiation that escapes plasma without being scattered, (2) the component Comptonized in the hot corona, and (3) the component Comptonized in the hot inner flow.

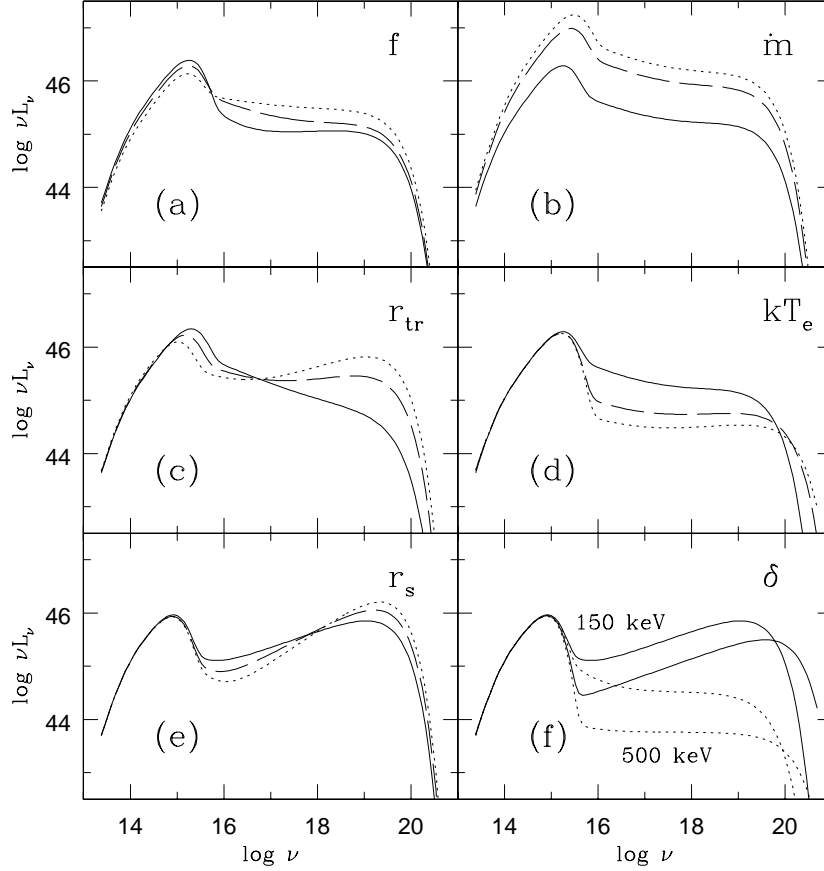


Fig. 2.— Spectra computed in geometry with the hot inner flow. Unless stated differently, the fixed parameters account for  $M=10^{10} M_\odot$ ,  $\dot{m}=0.1$ ,  $f=0.5$ ,  $r_{\text{tr}}=7 R_S$ ,  $r_s = r_{\text{tr}}$ ,  $kT_e = 150$  keV, and  $\delta = 1$ . The panels show the dependence of the following model parameters: (a) the fraction of energy dissipated in the clouds,  $f=0.1$  (solid curve),  $0.5$  (dashed curve), and  $0.9$  (dotted curve); (b) the accretion rate,  $\dot{m}=0.1$  (solid curve),  $0.5$  (dashed curve), and  $0.9$  (dotted curve); (c) the transition radius,  $r_{\text{tr}} = 5R_S$  (solid curve),  $10R_S$  (dashed curve), and  $20R_S$  (dotted curve)  $R_S$ ; (d) the electron temperature,  $kT_e=150$  (solid curve),  $350$  (dashed curve), and  $500$  (dotted curve) keV; (e) the semiminor axis of the ellipsoidal flow,  $r_s = 25R_S$  (solid curve),  $10R_S$  (dashed curve),  $5R_S$  (dotted curve), with  $r_{\text{tr}} = 25R_S$ ; (f) the hot inner flow efficiency correction,  $\delta = 1$  (solid curves), and  $\delta < 1$  (dotted curves), for electron temperature of  $150$  (upper curves) and  $500$  keV (lower curves).

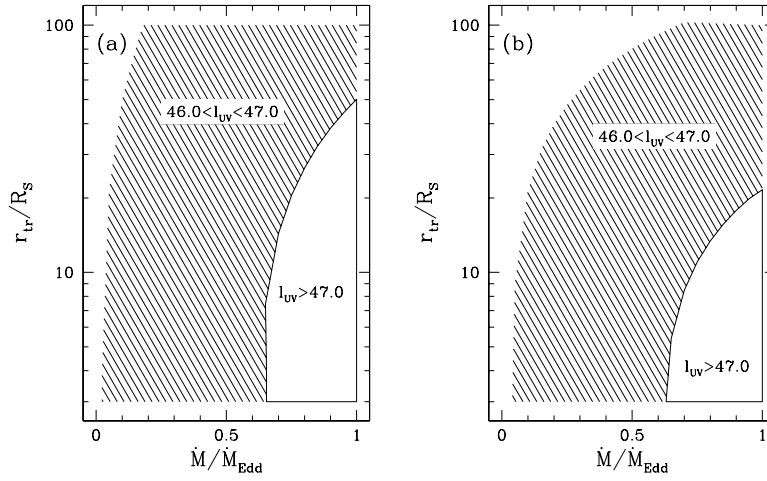


Fig. 3.— Dependence of the optical/UV luminosity on the disk truncation radius,  $r_{\text{tr}}$ , and the accretion rate,  $\dot{m}$ , for (a)  $\delta = 1$  and (b)  $\delta < 1$  (low-efficiency flow). The shaded regions produce spectra with UV luminosity  $46.0 < l_{\text{UV}} < 47.0$ . The solid curves enclose the part of parameter space with  $l_{\text{UV}} > 47.0$ . The computations were done for a black hole mass of  $10^{10} M_{\odot}$ , the fraction of energy released in the corona of  $f = 0.1$ , and the electron temperature of  $kT_e = 150$  keV. The result does not depend on the electron temperature. If the corona becomes stronger ( $f$  increases), the region with  $l_{\text{UV}} > 47.0$  disappears from the plot, and the most luminous objects cannot be fitted unless  $M > 10^{10} M_{\odot}$ .

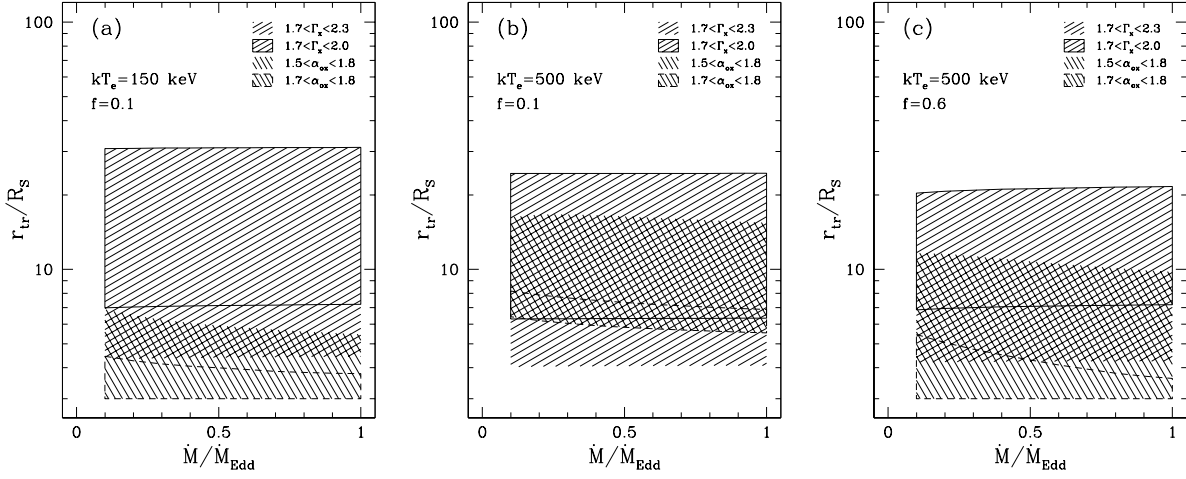


Fig. 4.— Results for geometry with efficient, hot, spherical inner flow ( $\delta = 1$ ,  $r_s = r_{\text{tr}}$ ; Section 2.3), showing the overlapping of regions yielding  $1.5 < \alpha_{\text{ox}} < 1.8$  and  $1.7 < \Gamma < 2.3$ . The solid curve encloses the part of the parameter space with the hardest spectra ( $\Gamma < 2$ ). The dashed curve encloses the region with the X-ray quietest spectra ( $\alpha_{\text{ox}} > 1.7$ ). The contours are calculated for  $kT_e = 150$  keV (a) and 500 keV (b and c), and a fraction of energy dissipated in the corona of  $f = 0.1$  (a and b), and  $f = 0.6$  (c). The overlapping exists for  $r_{\text{tr}} \leq 15 R_S$ . For electron temperatures  $\leq 150$  keV, the model can produce relatively soft and X-ray loud spectra with  $\Gamma \sim 2.0 - 2.3$ , and  $\alpha_{\text{ox}} \sim 1.5 - 1.7$  (a). For higher electron temperatures, harder ( $\Gamma < 2.0$ ) and X-ray quieter ( $\alpha_{\text{ox}} \sim 1.7 - 1.8$ ) spectra can be obtained (b). For a stronger corona and high electron temperature, the model gives either hard or X-ray quiet spectra (c). The computations were done for a black hole mass of  $10^{10} M_\odot$ .

Table 1. Modeling the SED of high- $z$  RQQs. Efficient Inner Flow.

OBJECT	$m^a$	$\dot{m}^b$	$f^c$	$\delta = 1$		$kT_e^e$	$\tau_c^f$	$\tau_s^f$	$\Gamma_{\text{fit}}^g$	$\alpha_{\text{UV}}^h$	$\alpha_{\text{ox}}^i$
				$r_{\text{tr}}^d$	$r_s^d$						
BRI0103+0032	$5.5 \times 10^9$	0.9	0.1	10	10	520	0.01	0.11	1.84	-0.28	1.57
	$1 \times 10^{10}$	0.45	0.1	10	10	480	0.02	0.13	1.84	-0.62	1.59
	$8 \times 10^9$	0.48	0.1	7	7	290	0.04	0.22	1.96	-0.35	1.57
	$1 \times 10^{10}$	0.35	0.1	8	5.5	370	0.03	0.20	1.84	-0.52	1.58
	$8.5 \times 10^9$	0.42	0.1	6	4	230	0.06	0.32	1.96	-0.34	1.57
PSS0248+1802	$1 \times 10^{10}$	0.65	0.1	7	7	240	0.05	0.29	1.96	-0.33	1.52
	$1 \times 10^{10}$	0.64	0.1	6	4	190	0.08	0.40	1.97	-0.28	1.52
BRI1033-0327	$1 \times 10^{10}$	0.31	0.1	5	5	108	0.17	0.59	2.19	-0.33	1.53
	$1 \times 10^{10}$	0.54	0.7	5	5	375	0.08	0.14	2.19	-0.34	1.53
	$1 \times 10^{10}$	0.44	0.56	$r_{\text{in}}$	$r_{\text{in}}$	252	0.12	...	2.39	-0.29	1.53
	$1.5 \times 10^{10}$	0.27	0.56	$r_{\text{in}}$	$r_{\text{in}}$	230	0.14	...	2.39	-0.49	1.55
	...	...	...	...	...	...	...	...	...	...	...
PSS1057+4555	$1.3 \times 10^{10}$	1	0.1	9	9	700	0.01	0.06	1.86	-0.41	1.70
	$1.2 \times 10^{10}$	0.98	0.1	7	7	495	0.02	0.10	1.94	-0.28	1.70
	$1.2 \times 10^{10}$	1	0.1	7	4	570	0.01	0.10	1.84	-0.30	1.70
	$1.4 \times 10^{10}$	0.78	0.1	6	4	410	0.02	0.14	1.93	-0.32	1.70
PSS1317+3531	$6 \times 10^9$	0.26	0.1	5	5	115	0.16	0.55	2.19	-0.27	1.52
	$6 \times 10^9$	0.34	0.4	5	5	230	0.11	0.25	2.25	-0.27	1.52
	$7 \times 10^9$	0.32	0.61	$r_{\text{in}}$	$r_{\text{in}}$	275	0.11	...	2.36	-0.30	1.52
	$1 \times 10^{10}$	0.21	0.61	$r_{\text{in}}$	$r_{\text{in}}$	260	0.12	...	2.36	-0.46	1.55
	...	...	...	...	...	...	...	...	...	...	...
SDS1030+0524	$5 \times 10^9$	0.79	0.1	11	11	1390	0.002	0.02	1.82	-0.34	1.79
	$1 \times 10^{10}$	0.38	0.1	11	11	1310	0.003	0.02	1.82	-0.76	1.81
	$7 \times 10^9$	0.45	0.1	7.2	4	850	0.01	0.05	1.82	-0.37	1.79
	$1 \times 10^{10}$	0.3	0.1	7.2	4	800	0.01	0.05	1.82	-0.56	1.80
	SDS1204-0021	$7 \times 10^9$	0.65	0.1	9	9	930	0.005	0.04	1.86	-0.36
$1 \times 10^{10}$		0.44	0.1	9	9	880	0.01	0.04	1.86	-0.56	1.77
$7 \times 10^9$		0.6	0.1	7	4	750	0.01	0.06	1.84	-0.29	1.77
PSS1443+2724	$1 \times 10^{10}$	0.39	0.1	7	4	690	0.01	0.07	1.84	-0.47	1.77
	PSS1443+2724	$5 \times 10^9$	0.65	0.1	9	9	590	0.01	0.08	1.87	-0.29
$6 \times 10^9$		0.46	0.1	7	7	400	0.02	0.14	1.95	-0.30	1.64
$1 \times 10^{10}$		0.26	0.1	7	7	380	0.03	0.15	1.95	-0.56	1.66
$6 \times 10^9$		0.48	0.1	7.3	5	450	0.02	0.13	1.87	-0.32	1.64
$6 \times 10^9$		0.44	0.1	6	4	330	0.03	0.19	1.94	-0.26	1.64
$1 \times 10^{10}$		0.25	0.1	6	4	310	0.04	0.21	1.94	-0.52	1.66

<sup>a</sup>Black hole mass in Solar masses,  $M_{\odot}$

<sup>b</sup>Accretion rate in Eddington units,  $\dot{M}_{\text{Edd}}$



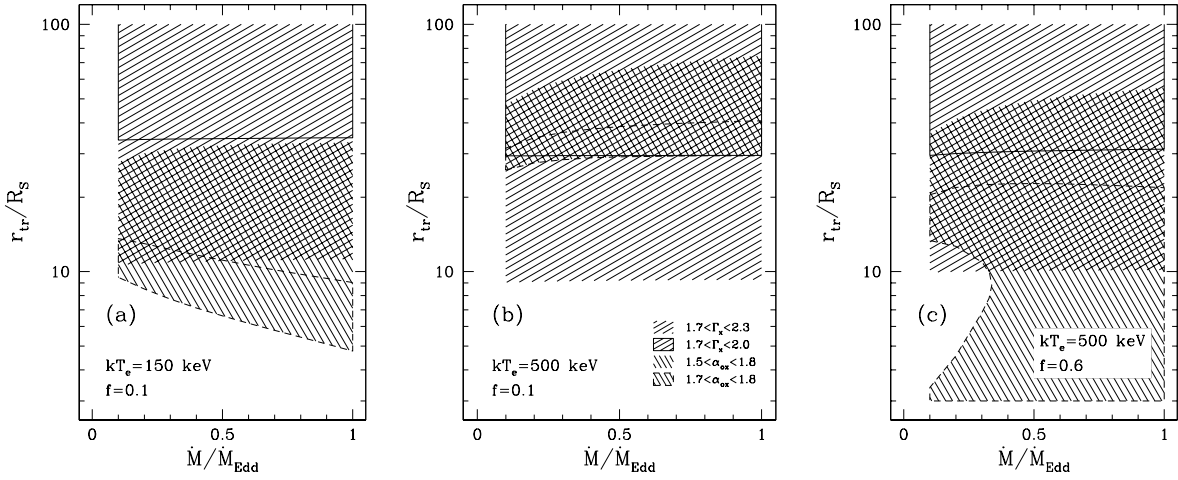


Fig. 5.— Results for geometry with low-efficiency, hot, spherical inner flow ( $\delta < 1$ ,  $r_s = r_{\text{tr}}$ ; Section 2.4), showing the overlapping of regions with  $1.5 < \alpha_{\text{ox}} < 1.8$  and  $1.7 < \Gamma < 2.3$ . The overall trends are similar to those illustrated in Figure 4. However, the truncation radius is now  $\sim 10 - 70 R_s$ , depending on the other parameters. The hardest and X-ray quietest spectra are produced for  $r_{\text{tr}} \sim 30 - 40 R_s$  and high electron temperatures (b). The computations were done for a black hole mass of  $10^{10} M_{\odot}$ .

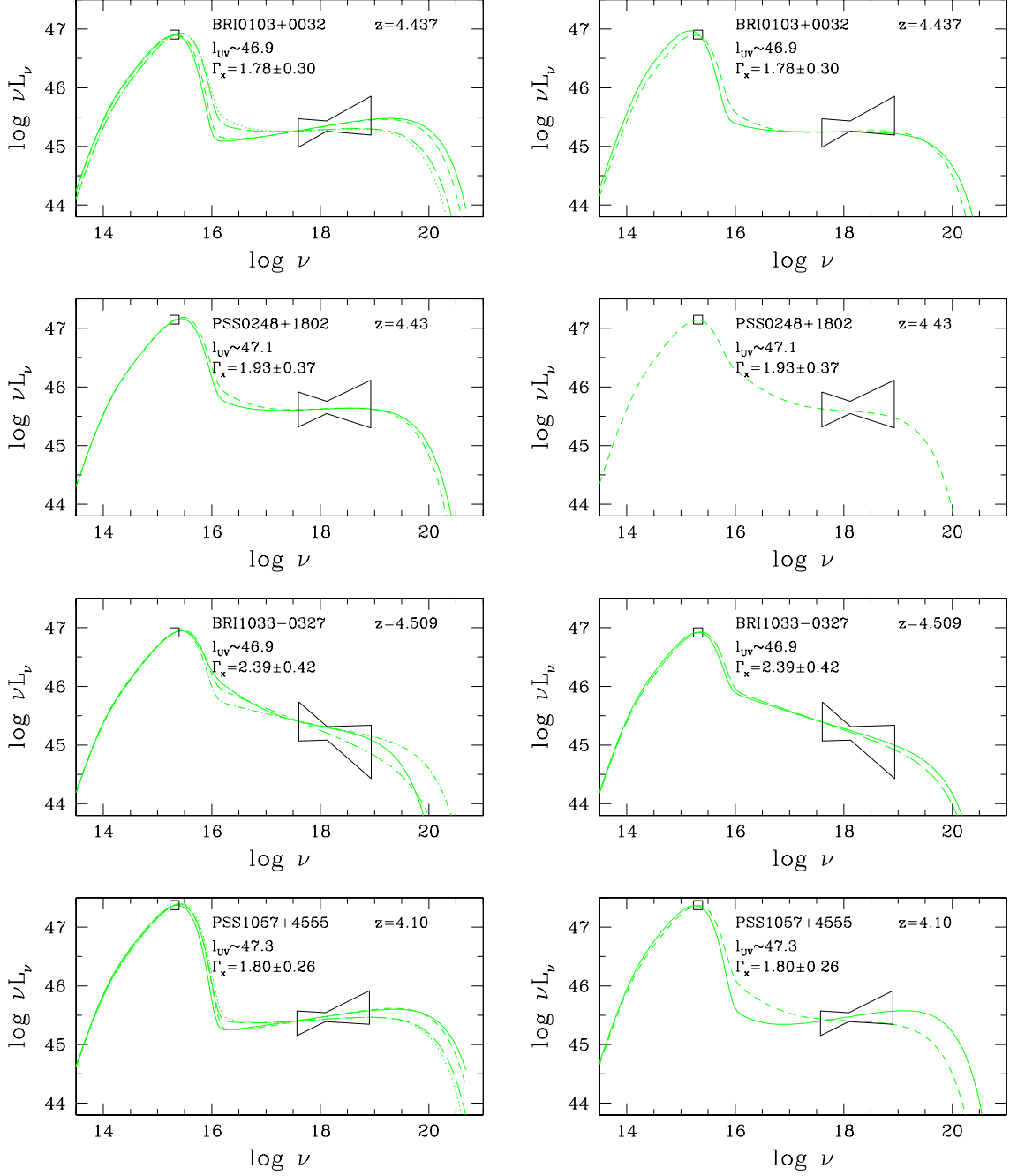


Fig. 6.— Modeling the objects from the B03 sample. *Left:* Hot semispherical flow ( $\delta=1$ ). *Right:* Low-efficiency semispherical flow ( $\delta < 1$ ). The curves show the following cases:  $r_{tr} = r_s$  (solid, long-dashed, dot-dashed curves),  $r_{tr} > r_s$  (dashed and dotted curves),  $f > 0.1$  (dot-dashed curves), and plane-parallel geometry (dash-long-dashed curves). Fit parameters are listed in Tables 1 and 2.

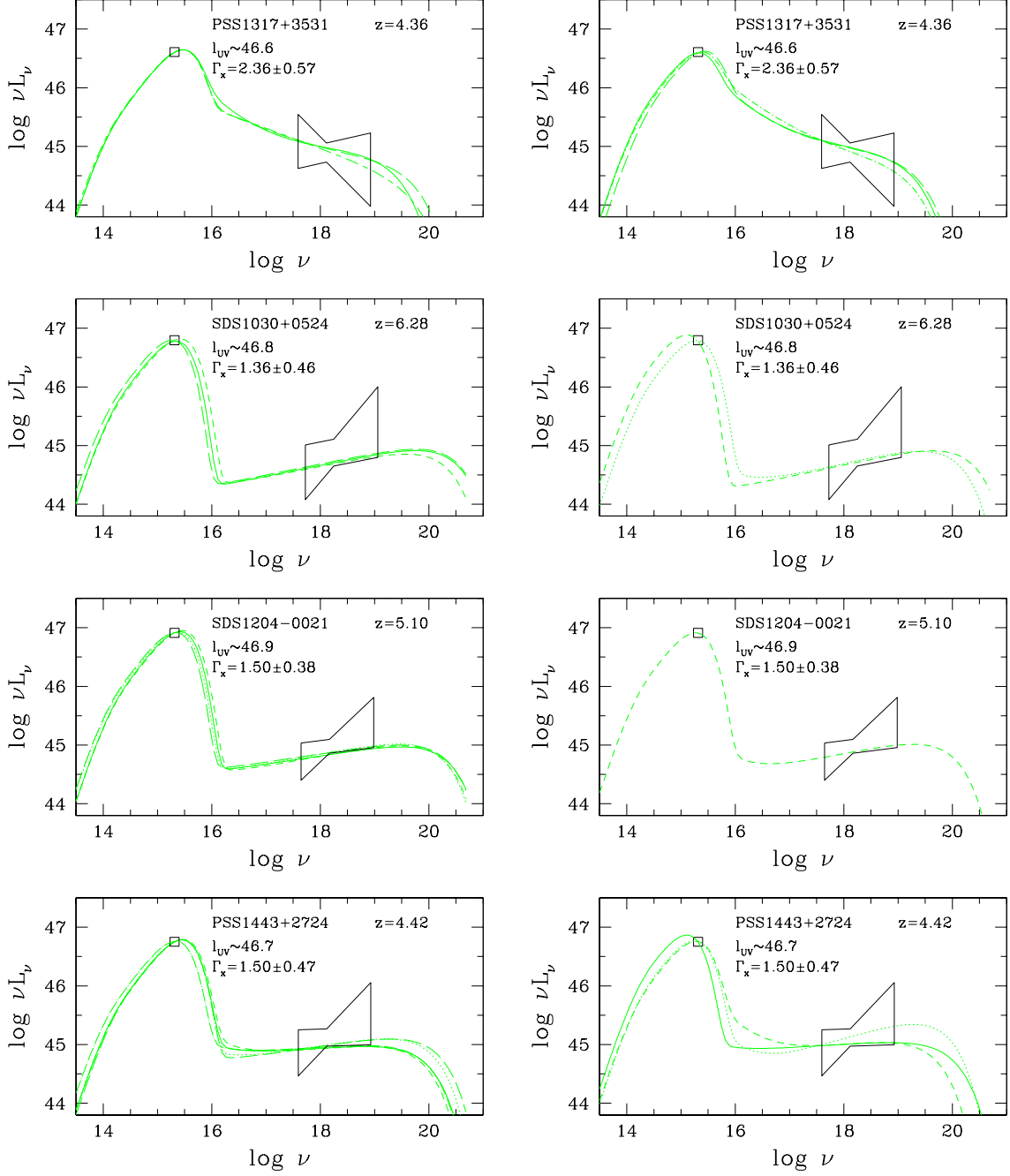


Fig. 7.— Modeling the objects from the B03 sample. *Left*: Hot semispherical flow ( $\delta=1$ ). *Right*: Low-efficiency semispherical flow ( $\delta < 1$ ). The curves show the following cases:  $r_{tr}=r_s$  (solid, long-dashed, and dot-long-dashed curves),  $r_{tr} > r_s$  (dashed and dotted curves),  $f > 0.1$  (dot-dashed curves), and plane-parallel geometry (dash-long-dashed curves). Fit parameters are listed in Tables 1 and 2.

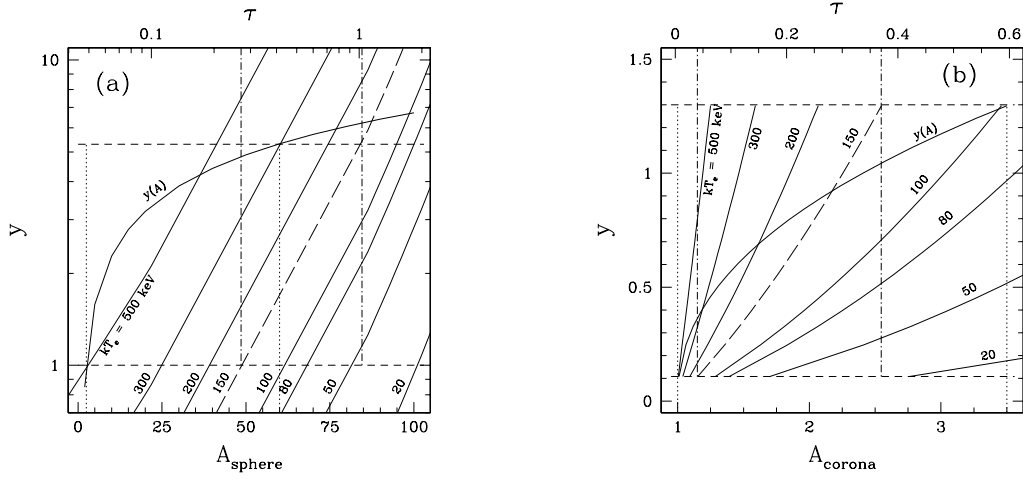


Fig. 8.— Hot plasma parameters in the model with no reduction in efficiency ( $\delta = 1$ ), and spherical inner flow ( $r_{tr} = r_s$ ) for (a)  $r < r_{tr}$  (the inner flow) and (b)  $r > r_{tr}$  (the corona). The thick solid curves show the dependence of the Compton parameter,  $y$ , on the amplification factor,  $A$ , obtained by combining eqs. (8) and (9). Vertical dotted lines (at [a]  $A = 2.5$  and  $A = 60$  and [b]  $A = 1$  and  $A = 3.5$ ) show the range of  $A$  possible to obtain from the model. The horizontal dashed lines show the corresponding range of  $y$ . Solid lines illustrate the relation between the Compton parameter,  $y$ , the optical depth,  $\tau$  (*upper axis*), and the electron temperature,  $kT_e$  (eq. [7]). The range of  $y$  marked by the horizontal lines, corresponds to the range of  $\tau$  for a given  $kT_e$ . For illustration, the range of  $\tau$  for  $kT_e = 150$  keV is shown by dash-dotted lines.

<sup>c</sup>Fraction of gravitational energy dissipated in the corona above the disk

<sup>d</sup>Disk truncation radius,  $r_{\text{tr}}$ , and the semi-minor axis of the ellipsoidal flow,  $r_s$ , in Schwarzschild units,  $R_S$

<sup>e</sup>Plasma temperature in keV

<sup>f</sup>Optical depth of corona,  $\tau_c$ , and semispherical flow,  $\tau_s$

<sup>g</sup>X-ray photon index allowed to vary within the  $1\sigma$  confidence interval (we do not list  $l_{\text{UV}}$  from fits since its value was fixed at that observed)

<sup>h</sup>UV index between 1450 and 2500 Å in the rest frame

<sup>i</sup>X-ray loudness

Table 2. Modeling the SED of high- $z$  RQQs: Low-Efficiency Inner Flow

OBJECT	$m^a$	$\dot{m}^b$	$f^c$	$\delta < 1$		$kT_e^e$	$\tau_c^f$	$\tau_s^f$	$\Gamma_{\text{fit}}^g$	$\alpha_{\text{UV}}^h$	$\alpha_{\text{ox}}^i$
				$r_{\text{tr}}^d$	$r_s^d$						
BRI0103+0032	$8.5 \times 10^9$	1.4	0.1	28	28	290	0.04	0.20	2.00	-1.17	1.66
	$7.5 \times 10^9$	1	0.1	19	9	200	0.07	0.37	1.96	-0.82	1.62
PSS0248+1802	...	...	...	...	...	...	...	...	...	...	...
	$1 \times 10^{10}$	1	0.1	15	7	105	0.18	0.71	2.01	-0.65	1.55
BRI1033-0327	$9 \times 10^9$	0.86	0.1	12	12	280	0.11	0.17	2.28	-0.62	1.56
	$9 \times 10^9$	0.71	0.6	9	9	270	0.11	0.15	2.33	-0.48	1.55
PSS1057+4555	...	...	...	...	...	...	...	...	...	...	...
	$1.5 \times 10^{10}$	1.3	0.1	15.5	4	310	0.04	0.25	1.86	-0.82	1.73
PSS1317+3531	$5 \times 10^9$	0.53	0.1	15	15	90	0.21	0.66	2.23	-0.58	1.54
	$3 \times 10^9$	0.98	0.1	15	15	110	0.17	0.54	2.23	-0.31	1.52
SDS1030+0524	$5 \times 10^9$	0.48	0.15	12	12	90	0.25	0.61	2.36	-0.46	1.54
	...	...	...	...	...	...	...	...	...	...	...
SDS1204-0021	$1 \times 10^{10}$	1	0.1	27	10	920	0.005	0.04	1.80	-1.46	1.87
	$6 \times 10^9$	0.93	0.1	17	4	500	0.02	0.13	1.80	-0.70	1.80
PSS1443+2724	...	...	...	...	...	...	...	...	...	...	...
	$8 \times 10^9$	0.88	0.1	16	4	425	0.02	0.16	1.83	-0.77	1.79
	$8 \times 10^9$	1.4	0.1	35	35	460	0.02	0.11	1.95	-1.50	1.72
	$7 \times 10^9$	0.65	0.1	15	5	200	0.07	0.39	1.95	-0.74	1.65
	$6 \times 10^9$	1	0.1	20	4	290	0.04	0.34	1.75	-0.82	1.65

<sup>a</sup>Black hole mass in Solar masses,  $M_\odot$

<sup>b</sup>Accretion rate in Eddington units,  $\dot{M}_{\text{Edd}}$

<sup>c</sup>Fraction of gravitational energy dissipated in the corona above the disk

<sup>d</sup>Disk truncation radius,  $r_{\text{tr}}$ , and the semi-minor axis of the ellipsoidal flow,  $r_s$ , in Schwarzschild units,  $R_g$

<sup>e</sup>Plasma temperature in keV

<sup>f</sup>Optical depth of corona,  $\tau_c$ , and semi-spherical flow,  $\tau_s$

<sup>g</sup>X-ray photon index allowed to vary within the  $1\sigma$  confidence interval (we do not list  $l_{\text{UV}}$  from fits since its value was fixed at that observed)

<sup>h</sup>UV index between 1450 and 2500 Å in the rest frame

<sup>i</sup>X-ray loudness